Visualization and Analysis of Whole Depot Adipose Tissue Innervation

Jake W. Willows[1], Magdalena Blaszkiewicz[1,2], Amy Lamore[3], Samuel Borer[1], Amanda L. Dubois[3], Emma Garner[1], William P. Breeding[4], Karissa B. Tilbury[2,4], Andre Khalil[2,4,5], Kristy L. Townsend[1,2*]

[1]School of Biology and Ecology, University of Maine, Orono ME
[2]Graduate School of Biomedical Science and Engineering, University of Maine, Orono ME
[3]School of Molecular and Biomedical Sciences, University of Maine, Orono ME
[4]Department of Chemical and Biomedical Engineering, University of Maine, Orono ME
[5]CompuMAINE Laboratory, University of Maine, Orono ME

*Corresponding Author – please direct all correspondence and requests for materials to:

kristy.townsend@maine.edu; 207-581-2541
5735 Hitchner Hall, Rm 301, Orono ME 04469

Abstract

Adipose tissue requires neural innervation in order to regulate important metabolic functions. Though seminal work on adipose denervation has underscored the importance of adipose-nerve interactions in both white (energy storing) and brown (energy expending) adipose tissues, much remains a mystery. This is due, in part, to the inability to effectively visualize the various nerve subtypes residing within these tissues and to gain a comprehensive quantitation of neurite density in an entire depot. With the recent surge of advanced imaging techniques such as light sheet microscopy and optical clearing procedures, adipose tissue imaging has been reinvigorated with a focus on three-dimensional analysis of tissue innervation. However, clearing techniques are time consuming, often require solvents caustic to objective lenses, alter tissue morphology, and greatly reduce fluorophore lifespan. Not only are current methods of imaging wholemount adipose tissues inconvenient, but often attempts to quantify neurite density across physiological or pathophysiological conditions have been limited to representative section sampling. We have developed a new method of adipose tissue neurite imaging and quantitation that is faster than current clearing-based methods, does not require caustic chemicals, and leaves the tissue fully intact. Maintenance of a fully intact depot allowed for tiling z-stacks and producing maximum intensity projections of the entire adipose depot, which were then used to quantify neurite density across the tissue. With this processing method we were able to characterize the nerves, nerve-subtypes, and neurovascular interactions within the inguinal subcutaneous white adipose tissue in mice using up to five fluorescent channels at high resolution. We also utilized second harmonic generation, which provides label-free imaging, to investigate collagen fiber abundance in adipose of obese mice.

Introduction:

Historically overlooked as a location of diverse peripheral innervation [1], the adipose organ was most prominently inspected for innervation in the mid 1960's when sympathetic nerve fibers were visualized within brown adipose tissue (BAT) [2]. BAT nerves were later comprehensively investigated by T.J. Bartness [3]. Energy expending BAT was the first adipose tissue to be identified as being highly innervated due to its important role in thermogenesis [4], which requires significant sympathetic input [2, 5, 6]. Sensory innervation has also been documented in BAT, particularly around vasculature, and has been proposed to play a role in lipolysis [7]. More recently white adipose tissue (WAT), associated more with energy storage, was demonstrated to be highly innervated by sympathetic [8, 9] and sensory nerves [5, 10], but not parasympathetic [11] nerves.

In order to visualize adipose innervation, it had been common practice to slice adipose tissue into 7um-10um thick sections and immunolabel for various neuronal markers [11-14], such as the sympathetic marker tyrosine hydroxylase (TH), the rate-limiting enzyme for synthesis of catecholamine neurotransmitters such as norepinephrine. A number of important findings emerged from this practice, but it was not without limitations. Thin sections of tissue reduce peripheral nerves to puncta, leaving investigators unable to accurately determine arborization or the ability to quantify innervation across an intact tissue. Importantly, our laboratory has revealed a new map of adipose anatomy in the inguinal subcutaneous white adipose tissue (i-scWAT) depot, and we and others have demonstrated that the pattern of innervation in scWAT is heterogeneous [15], thus warranting a more comprehensive look at adipose innervation across an intact depot and changes that may occur with physiological or pathophysiological stimuli.

The limitations of thin-slice immunostaining of adipose nerves did not go unnoticed, which resulted in the emergence of several methods for imaging and quantifying innervation within whole adipose depots [15-21]. However, even the new and improved methods also are not without their flaws. All of the current whole depot imaging methods require optical clearing and refractive index matching to visualize tissue innervation. Optical clearing typically alters tissue morphology by either shrinking, expanding, or hardening the tissue, or it greatly limits fluorophore lifespan to less than three days. Furthermore, some of the most effective methods of tissue clearing use caustic chemicals that require specialized objective lenses (ie: "BABB-safe") for microscopy. These issues with clearing techniques have been extensively reviewed in

multiple organs [22-24]. The current methods also typically rely on quantifying only a few small representative three-dimensional tissue sections, which misses the heterogeneity and regional anatomy of the intact tissue. The regional variation in neurite density in scWAT [15, 19], cannot be accurately reduced to a few representative images or a small tissue block.

To mitigate all of the issues outlined above, we have developed a whole mount imaging technique that does not require optical clearing or tissue sectioning and can be imaged using standard confocal microscopy and quantified using code that we have made publicly available. Our technique maintains an intact adipose depot and allows for detailed visualization of up to five fluorescent channels at a time at high resolution. This technique has been extensively tested with direct (conjugated antibodies) and indirect (primary and secondary antibodies) fluorescent labeling of various neuronal markers, as well as with mouse lines with fluorescent neuronal reporters. We have optimized our whole mount method for the pan-neuronal markers PGP9.5 [25, 26] and β3-tubulin [27, 28]; the sympathetic nerve marker, tyrosine hydroxylase (TH) [14]; markers for sensory innervation, advillin (AVIL) [29, 30] and Na_v 1.8 [31]; myelination marker myelin protein zero (MPZ) [32]; and many others. This technique has also been optimized for various non-antibody based fluorescent labeling approaches such as nuclear labeling with DAPI and vascular labeling with Isolectin IB_4 (IB4). This has allowed us to further our understanding of scWAT in mice by characterizing the innervation that exists within this tissue with greater scrutiny, demonstrating neurovascular interactions, parenchymal innervation, and neuroimmune interactions.

Methods:

Cold exposure experiments

All cold exposure was carried out in a diurnal incubator (Caron, Marietta, OH, USA) at 5°C. Adult male C67BL/6J mice were housed two to a cage and either maintained at room temperature or continuously cold exposed for 7 days. Inguinal and/or axillary scWAT was collected for wholemount tissue processing.

Mouse adipose tissue collection and processing for immunofluorescence

Mice were euthanized using CO_2 followed by cervical dislocation. Whole scWAT depots were carefully removed to remain fully intact and immediately fixed in 2% PFA at 4°C for 4hr-12hrs depending on thickness of tissue. The tissues were then rinsed for 10 minutes with 1X PBS w/ 10U/mL heparin, twice at 4°C. Tissues were incubated in blocking buffer (1XPBS/2.5% BSA/0.5-1% Triton) at 4°C at least overnight but no more than 7 days (depending on tissue

thickness) with blocking buffer replaced every 24hrs. After blocking period, tissues were flattened by being placed between two large glass slides bound tightly together with large binder clips, for 1.5hrs at 4°C to prevent tissues from drying out. Tissues were next incubated in either 0.1% Typogen Black for 20 minutes at room temperature on a rotator or TrueBlack® Lipofuscin Autofluorescence Quencher for 10 minutes at room temperature on a rotator. TrueBlack® was only used when using a 647nm fluorophore. At the end of incubation tissues were washed with 1X PBS w/ 10U/mL heparin on rotating platform at 4°C replacing PBS every 1hr for a total of 4-6hrs, or until all unbound stain was removed. Tissues were incubated with primary antibody for 48hrs at 4°C the following day tissues were washed with 1XPBS on a rotating platform at 4°C, replacing PBS every 1hr for a total of 4-6hrs followed by incubation with secondary fluorescent antibodies overnight. Tissues were then again washed with 1XPBS on a rotating platform at 4°C, replacing PBS every 1hr for a total of 4-6hrs. Following the immunostaining steps, when applicable, tissues were incubated with 1ug/mL isolectin B_4 (IB4) (ThermoFischer, cat#:I32450 or cat#:I21413) diluted in HEPES buffer (pH 7.4), overnight at room temperature on a rotator. Tissues were then washed with 1XPBS on a rotating platform at room temperature for one hour twice. At this time, if DAPI co-staining was required, the tissues were incubated in 100ng/mL DAPI for 10 minutes at room temperature on a rotator. Tissues then received four 1hr washes in 1xPBS at room temperature. At the conclusion of washing steps tissues were placed on large glass slides medial side facing up. A few drops of glycerol based mounting media were added to the tissue and coverslip was placed on top. Glycerol based mounting media is required because aqueous based mounting fluid lacks the required viscosity to fully adhere the coverslip when dealing with whole mount adipose. Slides were weighted down for 3-7 days then sealed.

Whole mount confocal imaging

Fully intact scWAT depots were imaged with a 10x objective on a Leica TCS SP8 DLS (Leica Microsystems, Wetzler, Germany) microscope by tiling z-stacks across the full depth and area of the tissue. Whole depot images in this manuscript were scanned bidirectionally at either 400Hz or 600Hz, with line averaging ranging between 3-8, and z-step size ranging between 5-16 µm. Identical image acquisition settings were applied for all tissues within cohorts that received neurite density quantifications. Anywhere between 20,000-65,000 individual images were captured per tissue which ranged from 100-900 tiles. These tiles were then merged together and processed into a 2D maximum intensity projection image either in LASX (Leica imaging software) or in Fiji [33] if being used for quantification. Digital nerve bundle cross

sectioning was performed by using the XZY scanning mode. During cross-sectioning a 2.54x digital zoom was automatically applied to each image.

Image processing and neurite density quantification

Maximum intensity projections through the z-dimension (z-max projection) were generated for each tile individually using Fiji [33]. All single tile z-max projections were further processed using MATLAB x64 software (version 2018b, MathWorks). To remove low-frequency background noise, a 2D Gaussian smoothing kernel was used to convolve each z-max projection with a very large Gaussian blur using the *imgaussfilt* MATLAB command, with large standard deviation (~150), which was then subtracted from its corresponding original z-max projection. Next, a small gaussian blur (*imgaussfilt* with small standard deviation, ~2-3) was used on the (post background subtraction) image to broaden out the neurite signal slightly before thresholding the image. Next, a binary (black and white) thresholded mask was generated from the processed image. In the mask, only regions having an area larger than 40 pixels were kept for further analysis (using the *bwareaopen* MATLAB command). Then the *bwskel* MATLAB command was used to perform the skeletonizing procedure, with the added feature of removing any branches less than 4 pixels long. Total nerve length was calculated using values measured for each single-tile z-max projection. Total nerve arborization density was calculated as the ratio of total nerve length divided by the total viewing area, resulting in nerve length per square meter of tissue. To generate heat maps a csv file was generated with the topological positions and the associated arborization quantity of each tile using the HeatMapChart function.

Second harmonic generation imaging

All 2-photon microscopy studies used a modified Olympus FV300 system with an upright BX50WI microscopy stand (Olympus, Center Valley, Pennsylvania) and a mode-locked Ti:Sapphire laser (Chameleon, Coherent, Santa Clara, California). Laser power was modulated via an electro-optic modulator (ConOptics, Danbury, Connecticut). The fluorescence and SHG signals were collected in a non-descanned geometry using a single PMT (H7422 GaAsP, Hamamatsu, Hamamastu City, Japan). Emission wavelengths were separated from excitation wavelengths using a 665 nm dichoric beamsplitter followed by 582/64 nm and 448/20 nm bandpass filters for Alexa 488 and SHG signals respectively (Semrock, Rochester, New York). Images were acquired using circular polarization with excitation power ranging from 1- 50 mW

and a 40x 0.8 NA water immersion objective with 3x optical zoom with scanning speeds of 2.71s/frame. All images were 515 x 512 pixels with a field of view of 85 µm.

Results and Discussion

Whole Mount Technique

We have tested numerous clearing techniques with scWAT and BAT (Suppl. Fig. S1) which included ScaleA2 [34], BABB [35, 36], CUBIC [37], CUBIC CB-perfusion [37], iDISCO [38], uDISCO [39], UbasM [40], and a sucrose gradient method [41]. Each clearing method had its own set of trade-offs, with some methods distorting tissue morphology, limiting fluorescence lifespan, and requiring costly objective lenses to image (summarized in Suppl. Table 1). These pros and cons have been well documented in various other tissues [22-24]. To circumvent these issues, we developed a method of whole tissue processing, outlined in Fig. 1a, that allowed for imaging and quantifiable analysis of intact whole adipose depots for up to 5-separate fluorescent channels (Suppl. Fig. S2) and did not require optical clearing. With the development of our wholemount technique we have found that, contrary to popular belief, optical clearing of scWAT is not necessary to image the innervation of entire scWAT depots. Furthermore, our method is significantly more time efficient and more cost effective than optical clearing. This approach has allowed us to image entire tissue depots and construct 2D visualizations from 3D data acquisition (by tiling z-max projection images taken at low magnifications using a laser scanning confocal microscope (Fig. 1b)). Generating images of entire tissues through tiled z-max projections requires tens of thousands of images to be captured and can often take between 10-30hrs to complete. This number is highly variable and dependent on tissue area and thickness, the desired image quality, sampling granularity, and the number of fluorescent channels being used. Tiled z-max projections can be processed for quantification of nerve density (as described in Methods section) (Fig. 1c). Because a two-dimensional image is rendered from three-dimensional data, the length of the nerve fibers in the z-plane is lost. However, the data omitted is negligible by comparison and does not affect tissue to tissue comparisons. The protocols for tissue processing and script for quantifying neurite density have been made available at protocols.io and GitHub respectively (Fig. 1d).

Whole mount processing of inguinal and axillary scWAT was achieved by excising intact depots from the mouse and fixing in 2% PFA. Tissue z-depth was reduced significantly by flattening the tissue between 2 large glass slides with binder clips to apply pressure; in a process we've termed "z-depth reduction." By reducing the tissue thickness in the z-plane we were able to reduce tissue thickness with minimal tissue deformity or effects on relative tissue

anatomy (Fig. 2a). Z-depth reduction provided increased penetration of blocking reagents and antibodies which significantly reduced incubation times and allowed for the whole tissue to be mounted on a slide with coverslip.

An important benefit of flattening adipose tissue is greater penetration of blocking solutions, antibodies, and autofluorescence quenching solutions. For most imaging we used 0.1% Sudan Black B (henceforth referred to by the less racially-problematic term Typogen Black) to decrease tissue autofluorescence. Typogen Black staining has been used as a treatment to quench tissue autofluorescence for decades in 7-10 µm thick sections [42]. Tissue autofluorescence has always been a significant problem when imaging adipose due to the inherent autofluorescecent nature of lipids and lipofuscin that reside within it [43]. We applied this technique to the entire adipose depot to greatly reduce tissue autofluorescence in combination with DAPI, GFP, Cy3, and Cy5 excitation/emission filters (Fig. 2b). However, Typogen Black itself is highly fluorescent under far red excitation (illustrated using Cy5 filter in figure 2b) which makes it often necessary to quench autofluorescence with TrueBlack instead, which does not fluoresce as extensively with far red excitation (Fig. 2b-c). Red blood cells are also highly autofluorescent which made it necessary to implement washing steps that used 1X PBS with 10U/mL Heparin to help flush out remaining blood from vasculature (Fig. 2d). In other instances, the autofluorescent red blood cells can be exploited to visualize the larger blood vessels that are missed by IB4, as we did previously [15].

Uniform staining of large whole mount tissues has always been problematic due to the increased incubation times required for antibodies to completely diffuse throughout the tissue [44, 45]. Incubation times were reduced 1-2 days by reducing tissue thickness and increasing surface with z-depth reduction. Depth coding of immunostained scWAT following z-depth reduction indicated an even penetration of antibodies throughout the whole tissue (Fig. 2e) and in representative sections (Fig. 2f) for various fluorescent staining approaches including: directly labeled β3-tubulin, indirectly labeled TH, and IB4 staining.

Whole mount imaging allows for quantification of total depot innervation

Axillary scWAT depots taken from male C57BL/6J mice, housed at room temperature or underwent cold exposure at 5ºC for 7-days, were processed for whole mount imaging using the pan-neuronal marker PGP9.5 (Fig. 3a). The neurite densities per tile were then averaged for the entire area of the tissue for comparison among treatments. Quantification of images allowed for statistical analysis between experimental groups (Fig. 3b). This quantification approach is not limited to innervation assessments but can be applied to vasculature (ie: IB4) as well. Neurite

density per z-max tile was then portrayed as a heatmap for both inguinal and axillary scWAT depots to better visualize region specific differences in neurite densities (Fig. 3c).

Characterization of Peripheral Nerves in scWAT

Inguinal scWAT depot was co-stained with two different pan-neuronal markers (PGP9.5 and β3-tubulin), counterstained with DAPI to emphasize tissue cellular structure, and tiled images were z-max projected. Whole tissue imaging exhibited near-uniform staining of the largest nerve bundles by both pan-neuronal markers (Fig. 4a). Nerves are unevenly distributed throughout the tissue with the highest concentration of large nerve bundles present in the centermost third of the tissue surrounding the subiliac lymph node (SiLN) as reported previously [15]. Our imaging and analysis technique exceeds current methods because it takes the heterogenous nerve distribution into account by quantifying the entire tissue, not just representative sections. At greater magnification, z-max projection images showed an extensive network of neurons varying in diameter running throughout the tissue and surrounding adipocytes as well as vasculature (Fig. 4b) which averaged a combined neurite length of 25m per i-scWAT depot [15].

Again, there appears to be almost complete fluorescent overlap for each pan-neuronal marker, with slightly stronger staining of PGP9.5 on the smaller nerve fibers. Digital cross section imaging of large nerve bundles presented uniform staining throughout the bundles (Fig. 4c). DAPI stained nuclei can be seen both surrounding the nerve bundle and residing within it, in between the numerous nerve fibers. Since the nuclei of the neurons are located in the ganglia the presence of nuclei within the nerve bundle suggests the presence of supporting cells (e.g. Schwann cells) or potentially perineural adipocytes residing within the bundles. This technique was also used to visualize a nerve branching (Suppl. Fig. S2c). Variation in immunofluorescence staining between the two pan-neuronal markers can be attributed in part to variations in the labeling methods of each antibody. β3-tubulin was directly conjugated to a fluorophore while PGP9.5 required use of secondary fluorescent antibodies. The innate autofluorescent quality of adipose tissue, though greatly reduced by Typogen Black or TrueBlack® staining, is still visible and at its strongest when imaged at 488nm.

Transmission electron microscopy of scWAT sections revealed that nerves not only traverse through the tissue but may also come in direct contact with the adipocytes (Suppl. Fig. S3a-b). However, we have yet to confirm synapsing directly onto adipocytes, though potential synapses have been observed in the stromal vascular fraction (SVF) of perigonadal adipose tissue (Suppl. Fig. S4a) as well as on blood vessels (Suppl. Fig. S4b), and on myeloid lineage SVF cells in inguinal scWAT (Suppl. Fig. S4c) using the post-synaptic marker PSD95. In general, the

understanding of adipose tissue innervation has not extended to characterizing cellular interactions and whether they are synaptic or simply result from diffusion of neuropeptides and neurotransmitters from nearby free nerve endings.

To further characterize the nerves within scWAT, numerous immunostaining experiments were conducted by co-staining β3-tubulin with markers for either sympathetic nerves, sensory nerves, or myelination using the markers tyrosine hydroxylase (TH), advillin (AVIL), and myelin protein zero (MPZ) respectively. Whole depot imaging demonstrated fluorescence overlap of β3-tubulin and TH in the largest nerve bundles with extensive TH+ axons that spanned throughout the tissue (Fig. 5a). Nerve bundle digital cross sectioning showed that only about half of the axons in a given nerve bundle are TH+ (Fig. 5b). The small individual axons branching through the tissue, however, are nearly all TH+ (Fig. 5c), consistent with previous reports [11, 21]. Fluorescent imaging of inguinal scWAT from a sympathetic nerve reporter mouse (*TH-Cre-Rosa26-GFP)* had similar findings (Suppl. Fig. S5a).

Digital cross sectioning of AVIL+ nerve bundles revealed similar findings to cross sectioning TH+ bundles, with only about half of the axons within the bundle presenting as AVIL+ (Fig. 5d) further suggesting the presence of mixed nerves in adipose. It is worth noting that the AVIL antibody used here was observed to mark structural proteins in some large blood vessels as well which accounted for the presence AVIL+ regions that were β3-tubulin- when viewed as a tiled image. At greater magnification these large blood vessels did not interfere with imaging and the lack of AVIL+ nerve fibers became apparent. Due to this, AVIL would appear to be a less-than-ideal marker for quantifying sensory innervation in conditions that may also alter vascularity. It is thought at this time that an AVIL reporter or a Na_v 1.8 reporter would be a far superior method of labeling sensory axons and a more comprehensive assessment remains to be completed.

Na_v 1.8-Cre x tdTomato reporter mice were also used to investigate the presence of sensory innervation in scWAT. Na_v 1.8 marks sodium channels specific to sensory nerves [31] and fluorescence imaging showed a number of Na_v 1.8+ sensory nerves throughout the tissue (Suppl. Fig. S5b), both large bundles and smaller parenchymal fibers, which compliments current literature that suggests sensory innervation plays a significant role in WAT metabolic function [14, 46]. As observed with AVIL immunostaining, imaging of i-scWAT from *Na_v 1.8-Cre x tdTomato* reporter mice also suggests the presence of mixed nerve bundles in this adipose depot (Suppl. Fig. S5b).

Whole depot staining with β3-tubulin and MPZ revealed that all of the large nerve bundles in scWAT are myelinated (Fig. 5e). In concordance with immunostaining, Luxol fast blue (myelin

stain) staining of whole inguinal scWAT depots was performed which showed that the most highly myelinated nerves traverse through or nearby the SiLN (Suppl. Fig. S5c). Digital cross sectioning of MPZ+ nerve bundles showed that all of the axons within the bundle are myelinated, with the greatest fluorescence intensity being on the exterior of the bundle (Fig. 5f), indicating that myelinated an non-myelinated axons are segregated in the bundle. Z-max projection imaging of parenchymal nerve fibers revealed that the majority of nerve endings are unmyelinated (Fig. 5g). TEM imaging was used to show both myelinated and unmyelinated neurites in contact with adipocytes (Suppl. Fig. S3a-b)

Our whole mount imaging technique has validated the presence of mixed bundle nerves residing in WAT shown previously [16] and allowed for further investigation by creating digital cross sections of these mixed bundles. High magnification z-max projections revealed that almost the entirety of neurons within the scWAT parenchyma are TH+. Only a small percentage of axons in the tissue are myelinated, however the contribution of myelinated versus unmyelinated axons to tissue function is currently unknown.

Neurovascular interaction in scWAT

The autonomic nervous system, comprised of sympathetic, parasympathetic, and sensory nerves, is required for regulating vascular tension [47] throughout the body, and WAT is no different. Sympathetic nerve fibers are responsible for vasoconstriction and parasympathetic fibers are responsible for vasodilation though it has been shown that WAT lacks parasympathetic innervation indicating that precise control of vasodilation is not required for WAT [11].

Neurovascular staining of whole depot scWAT was performed by co-staining with a pan-neuronal markers and IB4, a marker for vasculature, as it binds to erythrocytes and endothelial cells [48-52] and effectively marks vessels smaller than 200um in diameter. Wholemount axillary scWAT (a-scWAT) tiled z-max projections exposed a dense vascular network residing in the a-scWAT depot (Fig. 6a). In general, the highest concentration of large nerve bundles and large blood vessels are located within close proximity of one another. These observations are consistent with what we have observed in inguinal scWAT [15]. In contrast to neurites, capillaries appear homogenously expressed throughout the tissue (Fig. 6a). Close inspection of the neurovascular interactions within scWAT revealed three specific and reoccurring types of interactions (Fig. 6b): i) Large nerve bundles and blood vessels that run parallel to each other within the tissue but do not seem to interact otherwise, ii) Large nerve bundles that have a vascular supply providing nutrients; vasa nervorum, iii) Blood vessels that are highly innervated

by smaller nerves which regulate vasoconstriction; perivascular sympathetic plexus. TEM imaging revealed a small axon in the stromal vascular fraction in between adipocytes in close proximity to a capillary (Suppl. Fig. S3c). Sympathetic innervation of scWAT blood vessels was analyzed by co-staining β3-tubulin with TH and IB4. Small TH+ nerve fibers were found lining many of the vessels (Fig. 6c). Although small capillaries had significantly less innervation compared to larger arterioles, some TH+ nerves were found running along them. This supports the current literature that capillaries are relatively lacking in sympathetic innervation [53-55].

Not all nerves within the tissue are lining blood vessels; many can be found branching the gaps from one blood vessel to another or disassociated from the blood vessels entirely. The vasa nervorum, or the blood vessels supplying nutrients to the nerve bundle, were digitally cross sectioned to show a blood vessel branching around a nerve bundle which contained 2 sympathetic axons (Fig. 6d). Extensive innervation of arterioles could be found surrounding both large and small diameter vessels (Fig. 6e). Of the nerves running throughout scWAT, the majority MPZ+ nerves were found running along blood vessels as indicated by co-staining with β3-tubulin, MPZ, S100β (a Schwann cell marker), and IB4 (Fig. 6f) (Suppl. Fig. S3). Only one or two of the largest nerves lining each vessel tended to be myelinated. The smallest sympathetic projections that often engulfed many of the arterioles, when present, were found to be unmyelinated.

It is important to note several caveats with IB4 staining of vasculature. Mouse blood vessel diameter ranges from 250um to 4um dependent on type of vessel. Veins encompass the upper limit, while microvasculature such as capillaries encompass the lower limit [56]. Large diameter blood vessels (>100um) often lose their erythrocytes during tissue preparation which employs a heparin wash step to remove as much blood as possible to reduce the inherent autofluorescence associated with blood cells. However, erythrocytes tend to remain in the microvasculature even after these washes. Because of this, the microvasculature is doubly stained (erythrocytes and endothelium) whereas arteries and veins present only with stained endothelium. This reduction in fluorescence, most prominent in the largest vasculature, can even be seen starting as small as 50um in diameter though these vessels are still readily visible (figure 6). Also, large sensory nerve bundles, immunostained for AVIL, an actin binding protein expressed specifically in somatosensory neurons [29, 30], tended to be co-stained with IB4. IB4 binding sensory neurons has been reported in the literature [57, 58] and observed in supplemental figure S5d. However, due to tissue morphology, positively stained nerve bundles can be easily distinguished from the vasculature.

Second Generation Harmonic Imaging

We also attempted to visualize the changes to inguinal scWAT innervation of morbidly obese mice which we have demonstrated to have adipose neuropathy ($BTBR^{ob/ob}$); [15]. This proved technically difficult to accomplish using epifluorescent or standard confocal microscopy, due in part to the fibrotic nature of obese adipose tissue. However, with second generation harmonic label-free imaging using 2-photon microscopy, it was possible to visualize nerves and collagen within scWAT of $BTBR^{ob/ob}$ animals (Fig. 7). While collagen is abundant in both $BTBR^{+/+}$ and $BTBR^{ob/ob}$ animals, a greater degree of colocalization between collagen fibers and nerves is visible in $BTBR^{ob/ob}$ animals (Fig. 7a), likely contributing to our inability to image the adipose nerves successfully in this mouse model.

Conclusion

Taken together, the imaging techniques and data collected here reveal a rich and diverse neural innervation in mouse inguinal scWAT, likely indicating physiological roles that are yet to be uncovered. For example, differences in myelinated vs unmyelinated axons, heterogeneity of TH+ nerves, and the contribution of sensory nerves in adipose are yet to be clarified. In addition, the localization of true synapses or tissue junctions, versus release of nerve products from free nerve endings, and whether these exist on adipocytes or SVF cells, will also be important to uncover. The availability of new techniques allowing nerve visualization under various physiological and pathophysiological conditions will help the field advance an understanding of adipose innervation and brain-adipose communication, including neurovascular and neuroimmune contributions.

We have recently demonstrated diminished innervation of adipose tissue under circumstances of obesity, diabetes, and ageing, a condition we have called ‘adipose neuropathy’ [15]. ‘Neuropathy’ of adipose tissue (ie: a reduction in neurite density that may represent pathological nerve die-back) could have effects beyond the removal of sympathetic nerves releasing norepinephrine. Given that other nerve products, including from adipose tissue sensory nerves (ex: Substance P, VIP, CGRP, etc.) are found in adipose depots, the loss of proper innervation could also impact the physiological contributions of these neuromodulatory substances in adipose. Whether or not adipose sensory nerves directly communicate fuel status to the brain, perhaps in complement to endocrine factors such as leptin, is still an open question. In addition, how adipose nerves interact with vasculature versus parenchymal cells, including stromovascular cells, is also unexplored. Incoming sympathetic nerves may release

457 norepinephrine in order to affect vasoconstriction, and also to impact local adipocytes and
458 immune cells via synaptic and non-synaptic connections.
459
460
461
462
463
464

Acknowledgements

Dr. Benjamin Harrison of UNE for developing earlier iterations of whole depot innervation quantification method. Dr. Clarissa Henry of UMaine for Leica lightsheet confocal microscope training. Morganne Robinson, Thomas Szewczyk, Cory Johnson and James Miller for technical assistance. Dr. Ian Meng of The University of New England for gifting *$Na_v1.8$* reporter mice adipose tissues. Dr. Dustin Updike of MDI Biological Laboratory for assistance with pilot imaging studies. Dr. Seth Tyler and Kelly Edwards of UMaine for TEM technical assistance.

Author Contributions

JWW wrote the manuscript, created and optimized protocols, designed experiments, and conducted majority of microscopy studies. MB wrote the manuscript, designed experiments, and optimized protocols. EG conducted TEM experiments. AL and AD conducted clearing experiments. SB and AK developed neurite density quantification methods. PB and KT conducted 2-photon imaging. KLT wrote the manuscript, designed experiments, and oversaw the project.

Competing Interests

The authors declare no competing interests.

Data and Code Availability

Neurite density quantification and heat map generating code can be found on GitHub at https://github.com/ktownsendlab/willows_et_al-2019. Protocols used for this publication can be found on Protocols.io at dx.doi.org/10.17504/protocols.io.6nzhdf6. All other data is included in this manuscript.

Ethical Approval

All procedures and handling of animals were performed in accordance with the University of Maine's Institutional Animal Care and Use Committee (IACUC), to comply with the guidelines of the PHS Policy on Humane Care and Use of Laboratory Animals, and Guide for the Care and Use of Laboratory Animals. This study was approved by the University of Maine's IACUC, under protocol A2017-09-04.

499

500 **Figure Legends:**

501

502 **Figure 1: Wholemount tissue staining, imaging, and post-processing**. Diagram depicting
503 steps of wholemount tissue processing technique (a). 1.) An intact scWAT depot is carefully
504 excised from mouse postmortem. 2) Tissue fixed in 2% PFA at 4ºC for 16hr per 1.0g of adipose.
505 Tissue is then washed in 1X PBS (w/ Heparin 10u/mL) for four 1hr washes at 4ºC on rotator 3.)
506 Tissue is squished between large slides held together with binder clips for 1.5hr at 4ºC. 4)
507 Tissue is removed from slides and incubated in blocking solution (2.5% BSA, 1% Triton X-100,
508 in 1X PBS) on rotator at 4ºC for 1-7days with blocking solution replaced daily. 5) Tissue is
509 washed 1hr in 1X PBS (w/ Heparin 10u/mL) and incubated in 0.1% Typogen Black in 70% EtOH
510 for 20min, washed in 1X PBS (w/ Heparin 10u/mL) in 1hr increments at 4ºC on shaker until
511 Typogen Black run-off ceases. 6) Tissue is incubated in primary antibody solution at 4ºC on
512 rotator for 2 days. 7) Tissue is washed x4 again with 1x PBS and incubated in secondary
513 antibody solution at 4ºC on rotator overnight. 8) Tissue washed x4 with 1X PBS and mounted
514 on slide with glycerol based mounting fluid. Glass coverslip is applied and slide is placed under
515 significant weight for 3 days at room temp. 9.) Slide is sealed with nail polish and ready for
516 imaging (a). Tiled z-stacks were imaged for the entire tissue with either a 5x or 10x objective
517 and a 2D maximum projection image was rendered (b). Post processing of single tile z-max
518 projections for neurite density quantification (c). Each z-max projection tile was further
519 processed by subtracting the background away and adding light smoothing. Next a thresholded
520 mask was applied and the image was skeletonized. Total neurite length was calculated for each
521 tile and averaged for the entire viewing area (c.) Link to whole mount protocols and script for
522 quantification (d.)

523

524

525

526

527

528

Figure 2: Reduction tissue autofluorescence and depth coding. Z-depth reduction was performed on inguinal scWAT depot for comparison before and after (a). Subcutaneous WAT depots from *C57BL/6J* mice were whole depot processed and incubated in either Typogen Black or TrueBlack® for equal duration. Autofluorescence was evaluated for each blocking method for 4 different fluorescent filter cubes: DAPI, GFP/FITC, Cy3/TRITC, and Cy5 (b). Blocking methods were further compared for the Cy5 filter by staining the tissues with IB4 conjugated to a 647nm fluorophore. with either 10x objective (b) or both 4x and 40x objectives (c). scWAT depot stained with PGP9.5 (green) demonstrated significant reduction in orange vascular autofluorescence when tissues were washed with 1XPBS/10U/ml Heparin imaged at 10x and 4x (d). i-scWAT depot stained with β3-Tubulin, Tyrosine Hydroxylase (TH), and Isolectin IB_4 (IB4) and depth coded (e-f). Whole mount i-scWAT 3D depth coding was imaged with 10x objective (e) and high magnification representative 3D section was imaged with 63x objective(f). Images were captured on either Nikon E400 microscope (b-d) or Leica TCS SP8 DLS microscope (e-f).

Figure 3: Whole depot neurite quantification. Female *C57BL/6J* mice, aged 14-16wks, were either cold exposed (5ºC) (n=6) or at room temperature (n=4) for 7 days. Axillary scWAT depots were wholemount processed and stained with PGP9.5 and imaged with Leica TCS SP8 DLS confocal laser scanning microscope with 10x objective (a). Images were z-max projected and tiled (a). Neurite density quantification was performed across cohort for comparison and analyzed using a two-tailed Student's t-test (b). Alpha level 0.05, error bars are SEMs, p = 0.414 (b). Neurite density per z-max tile was calculated and used to generate a heatmap for inguinal scWAT and axillary scWAT depots (c).

Figure 4: Peripheral innervation of inguinal scWAT. Inguinal subcutaneous depots from *C57BL/6J* mice were wholemount processed and stained with DAPI to show tissue morphology and the pan-neuronal markers β3-Tubulin (green) and PGP9.5 (red) captured on Leica SP8 DLS microscope (a-c). Whole i-scWAT depot tiled z-max projections captured using 5x objective (a) with digital zoom-ins (i-ii). Representative images of small fiber innervation imaged as z-max projections with 63x objective (b). Nerve bundle imaged with 63x objective and digital cross sectioning performed with a 2.54x digital zoom (c).

Figure 5: Characterization of whole mount inguinal scWAT nerves. scWAT depots from *C57BL/6J* mice were wholemount processed and stained with β3-Tubulin (green) and either TH (red) (a-c), AVIL (red) (d), or MPZ (red) (e-g). Whole mount tiled z-max projections of i-scWAT (a,d) and a-scWAT (g) imaged with 10x objective. Nerve bundle cross sections imaged with 63x objective with a 2.54x digital zoom applied to the digital cross section rendering (b,e). Representative images of small fiber innervation imaged as z-max projections with 63x objective (c,f). All images captured on Leica TCS SP8 DLS microscope (a-g).

Figure 6: Neurovascular interaction within inguinal scWAT depot. i-scWAT from *C57BL/6J* mice were wholemount processed. Whole i-scWAT depot stained with PGP9.5 (green) and IB4 (white) was captured as tiled z-max projections imaged with 10x objective on Leica TCS SP8 DLS microscope (a). PGP9.5 (green) and IB4 (red) used to display the 3 categories of neurovascular interaction within scWAT, imaged on Nikon E400 with 10x, 4x, and 40x objectives respectively (b). Representative images of innervation of blood vessels imaged as z-max projections with 63x objective. β3-Tubulin (green), TH (red), IB4 (white) (b-d). Sympathetic innervation of small blood vessels (c). Vasa nervorum of i-scWAT nerve bundle imaged as z-max projection digitally cross sectioned with a 2.54x digital zoom (d). Large and small diameter blood vessel digital cross sectioning (e). 2.54x digital zoom applied to large diameter vessel cross section, 6.96x digital zoom applied to small diameter vessel cross section (e). Representative images of myelinated nerve fibers around vasculature imaged as z-max projections with 63x objective. DAPI (blue), β3-Tubulin (green), MPZ (yellow), S100β (red), IB4 (white) (f).

Figure 7: Second harmonic generation imaging. Two-photon microscopy was performed on immunofluorescent stained (PGP9.5) inguinal scWAT of $BTBR^{+/+}$ (WT) and $BTBR^{ob/ob}$ (MUT) animals (a). PGP9.5 was detected by excitation of AlexaFluor 488 at 800nm and emission collected using a 582 +/- 64nm filter. For detection of collagen, samples were excited at 890nm and the SHG signal was collected using a 448 +/-20nm filter. A 40x water immersion objective was used. IMARIS software was used to render 3D projections from z-stacks. Images are representative of N=3 WT/MUT, 12-week-old males.

References Cited

1. Blaszkiewicz, M., et al., *The Importance of Peripheral Nerves in Adipose Tissue for the Regulation of Energy Balance.* Biology (Basel), 2019. **8**(1).
2. Wirsen, C., *Adrenergic Innervation of Adipose Tissue Examined by Fluorescence Microscopy.* Nature, 1964. **202**: p. 913.
3. Cinti, S., et al., *Tim Bartness, Ph.D. (1953-2015).* Temperature (Austin), 2016. **3**(1): p. 31-8.
4. Fenzl, A. and F.W. Kiefer, *Brown adipose tissue and thermogenesis.* Horm Mol Biol Clin Investig, 2014. **19**(1): p. 25-37.
5. Bartness, T.J., C.H. Vaughan, and C.K. Song, *Sympathetic and sensory innervation of brown adipose tissue.* Int J Obes (Lond). 2010. **34 Suppl 1:S36-42.**: p. S36-S42.
6. Francois, M., et al., *Sympathetic innervation of the interscapular brown adipose tissue in mouse.* Ann N Y Acad Sci, 2019.
7. Garretson, J.T., et al., *Lipolysis sensation by white fat afferent nerves triggers brown fat thermogenesis.* Molecular metabolism, 2016. **5**(8): p. 626-634.
8. Foster, D.O., F. Depocas, and M. Zuker, *Heterogeneity of the sympathetic innervation of rat interscapular brown adipose tissue via intercostal nerves.* Can J Physiol Pharmacol, 1982. **60**(6): p. 747-54.
9. Foster, M.T. and T.J. Bartness, *Sympathetic but not sensory denervation stimulates white adipocyte proliferation.* Am J Physiol Regul Integr Comp Physiol, 2006. **291**(6): p. R1630-7.
10. Fishman, R.B. and J. Dark, *Sensory innervation of white adipose tissue.* Am J Physiol, 1987. **253**(6 Pt 2): p. R942-4.
11. Giordano, A., et al., *White adipose tissue lacks significant vagal innervation and immunohistochemical evidence of parasympathetic innervation.* Am J Physiol Regul Integr Comp Physiol, 2006. **291**(5): p. R1243-55.
12. Murano, I., et al., *Noradrenergic parenchymal nerve fiber branching after cold acclimatisation correlates with brown adipocyte density in mouse adipose organ.* J Anat, 2009. **214**(1): p. 171-8.
13. Vargovic, P., et al., *Adipocytes as a new source of catecholamine production.* FEBS.Lett., 2011. **585**(14): p. 2279-2284.
14. Shi, H., et al., *Sensory or sympathetic white adipose tissue denervation differentially affects depot growth and cellularity.* Am J Physiol Regul Integr Comp Physiol, 2005. **288**(4): p. R1028-37.
15. Blaszkiewicz, M., et al., *Neuropathy and neural plasticity in the subcutaneous white adipose depot.* PLoS One, 2019. **14**(9): p. e0221766.
16. Zeng, W., et al., *Sympathetic neuro-adipose connections mediate leptin-driven lipolysis.* Cell, 2015. **163**(1): p. 84-94.
17. Cao, Y., et al., *Three-dimensional volume fluorescence-imaging of vascular plasticity in adipose tissues.* Mol Metab, 2018. **14**: p. 71-81.
18. Cao, Y., H. Wang, and W. Zeng, *Whole-tissue 3D imaging reveals intra-adipose sympathetic plasticity regulated by NGF-TrkA signal in cold-induced beiging.* Protein Cell, 2018. **9**(6): p. 527-539.

19. Chi, J., et al., *Three-Dimensional Adipose Tissue Imaging Reveals Regional Variation in Beige Fat Biogenesis and PRDM16-Dependent Sympathetic Neurite Density.* Cell Metab, 2018. **27**(1): p. 226-236 e3.
20. Li, X., et al., *Co-staining Blood Vessels and Nerve Fibers in Adipose Tissue.* J Vis Exp, 2019(144).
21. Jiang, H., et al., *Dense Intra-adipose Sympathetic Arborizations Are Essential for Cold-Induced Beiging of Mouse White Adipose Tissue.* Cell Metab, 2017. **26**(4): p. 686-692 e3.
22. Richardson, D.S. and J.W. Lichtman, *Clarifying Tissue Clearing.* Cell, 2015. **162**(2): p. 246-257.
23. Azaripour, A., et al., *A survey of clearing techniques for 3D imaging of tissues with special reference to connective tissue.* Prog Histochem Cytochem, 2016. **51**(2): p. 9-23.
24. Seo, J., M. Choe, and S.Y. Kim, *Clearing and Labeling Techniques for Large-Scale Biological Tissues.* Mol Cells, 2016. **39**(6): p. 439-46.
25. Thompson, R.J., et al., *PGP 9.5--a new marker for vertebrate neurons and neuroendocrine cells.* Brain Res, 1983. **278**(1-2): p. 224-8.
26. Day, I.N. and R.J. Thompson, *UCHL1 (PGP 9.5): neuronal biomarker and ubiquitin system protein.* Prog Neurobiol, 2010. **90**(3): p. 327-62.
27. Draberova, E., et al., *Class III beta-tubulin is constitutively coexpressed with glial fibrillary acidic protein and nestin in midgestational human fetal astrocytes: implications for phenotypic identity.* J Neuropathol Exp Neurol, 2008. **67**(4): p. 341-54.
28. Latremoliere, A., et al., *Neuronal-Specific TUBB3 Is Not Required for Normal Neuronal Function but Is Essential for Timely Axon Regeneration.* Cell Rep, 2018. **24**(7): p. 1865-1879 e9.
29. Hasegawa, H., et al., *Analyzing somatosensory axon projections with the sensory neuron-specific Advillin gene.* J Neurosci, 2007. **27**(52): p. 14404-14.
30. Hunter, D.V., et al., *Advillin Is Expressed in All Adult Neural Crest-Derived Neurons.* eNeuro, 2018. **5**(5).
31. Bird, E.V., et al., *Correlation of Nav1.8 and Nav1.9 sodium channel expression with neuropathic pain in human subjects with lingual nerve neuromas.* Mol Pain, 2013. **9**: p. 52.
32. D'Urso, D., et al., *Protein zero of peripheral nerve myelin: biosynthesis, membrane insertion, and evidence for homotypic interaction.* Neuron, 1990. **4**(3): p. 449-60.
33. Schindelin, J., et al., *Fiji: an open-source platform for biological-image analysis.* Nat Methods, 2012. **9**(7): p. 676-82.
34. Hama, H., et al., *Scale: a chemical approach for fluorescence imaging and reconstruction of transparent mouse brain.* Nat Neurosci, 2011. **14**(11): p. 1481-8.
35. Dodt, H.U., et al., *Ultramicroscopy: three-dimensional visualization of neuronal networks in the whole mouse brain.* Nat Methods, 2007. **4**(4): p. 331-6.
36. Li, L., et al., *The functional organization of cutaneous low-threshold mechanosensory neurons.* Cell, 2011. **147**(7): p. 1615-27.
37. Susaki, E.A., et al., *Advanced CUBIC protocols for whole-brain and whole-body clearing and imaging.* Nat Protoc, 2015. **10**(11): p. 1709-27.
38. Renier, N., et al., *iDISCO: a simple, rapid method to immunolabel large tissue samples for volume imaging.* Cell, 2014. **159**(4): p. 896-910.
39. Pan, C., et al., *Shrinkage-mediated imaging of entire organs and organisms using uDISCO.* Nat Methods, 2016. **13**(10): p. 859-67.

40. Chen, L., et al., *UbasM: An effective balanced optical clearing method for intact biomedical imaging.* Sci Rep, 2017. **7**(1): p. 12218.
41. Brantschen, S., et al., *Regulatory effect of recombinant interleukin (IL)3 and IL4 on cytokine gene expression of bone marrow and peripheral blood mononuclear cells.* European Journal of Immunology, 1989. **19**: p. 2017-2023.
42. Schnell, S.A., W.A. Staines, and M.W. Wessendorf, *Reduction of Lipofuscin-like Autofluorescence in Fluorescently Labeled Tissue.* Journal of Histochemistry & Cytochemistry, 1999. **47**(6): p. 719-730.
43. Croce, A.C. and G. Bottiroli, *Autofluorescence spectroscopy and imaging: a tool for biomedical research and diagnosis.* Eur J Histochem, 2014. **58**(4): p. 2461.
44. Chung, K., et al., *Structural and molecular interrogation of intact biological systems.* Nature, 2013. **497**(7449): p. 332-7.
45. Kim, S.Y., et al., *Stochastic electrotransport selectively enhances the transport of highly electromobile molecules.* Proc Natl Acad Sci U S A, 2015. **112**(46): p. E6274-83.
46. Bartness, T.J. and M. Bamshad, *Innervation of mammalian white adipose tissue: implications for the regulation of total body fat.* Am J Physiol, 1998. **275**(5): p. R1399-411.
47. Sheng, Y. and L. Zhu, *The crosstalk between autonomic nervous system and blood vessels.* Int J Physiol Pathophysiol Pharmacol, 2018. **10**(1): p. 17-28.
48. Martinez-Santibanez, G., K.W. Cho, and C.N. Lumeng, *Imaging white adipose tissue with confocal microscopy.* Methods Enzymol, 2014. **537**: p. 17-30.
49. Ernst, C. and B.R. Christie, *Isolectin-IB 4 as a vascular stain for the study of adult neurogenesis.* J Neurosci Methods, 2006. **150**(1): p. 138-42.
50. Peters, B.P. and I.J. Goldstein, *The use of fluorescein-conjugated Bandeiraea simplicifolia B4-isolectin as a histochemical reagent for the detection of alpha-D-galactopyranosyl groups. Their occurrence in basement membranes.* Exp Cell Res, 1979. **120**(2): p. 321-34.
51. Ismail, J.A., et al., *Immunohistologic labeling of murine endothelium.* Cardiovasc Pathol, 2003. **12**(2): p. 82-90.
52. Gorakshakar, A.C. and K. Ghosh, *Use of lectins in immunohematology.* Asian J Transfus Sci, 2016. **10**(1): p. 12-21.
53. Rechthand, E., et al., *Distribution of adrenergic innervation of blood vessels in peripheral nerve.* Brain Res, 1986. **374**(1): p. 185-9.
54. Klabunde, R.E., *Cardiovascular physiology concepts*. 2nd ed. 2012, Philadelphia, PA: Lippincott Williams & Wilkins/Wolters Kluwer. xi, 243 p.
55. Thomas, G.D., *Neural control of the circulation.* Adv Physiol Educ, 2011. **35**(1): p. 28-32.
56. Müller, B., et al., *High-resolution tomographic imaging of microvessels.* Proc SPIE, 2008. **7078**: p. 70780B.
57. Fang, X., et al., *Intense isolectin-B4 binding in rat dorsal root ganglion neurons distinguishes C-fiber nociceptors with broad action potentials and high Nav1.9 expression.* J Neurosci, 2006. **26**(27): p. 7281-92.
58. Vulchanova, L., et al., *Cytotoxic targeting of isolectin IB4-binding sensory neurons.* Neuroscience, 2001. **108**(1): p. 143-55.

Figure 1: Adipose tissue processing, imaging, and quantification method

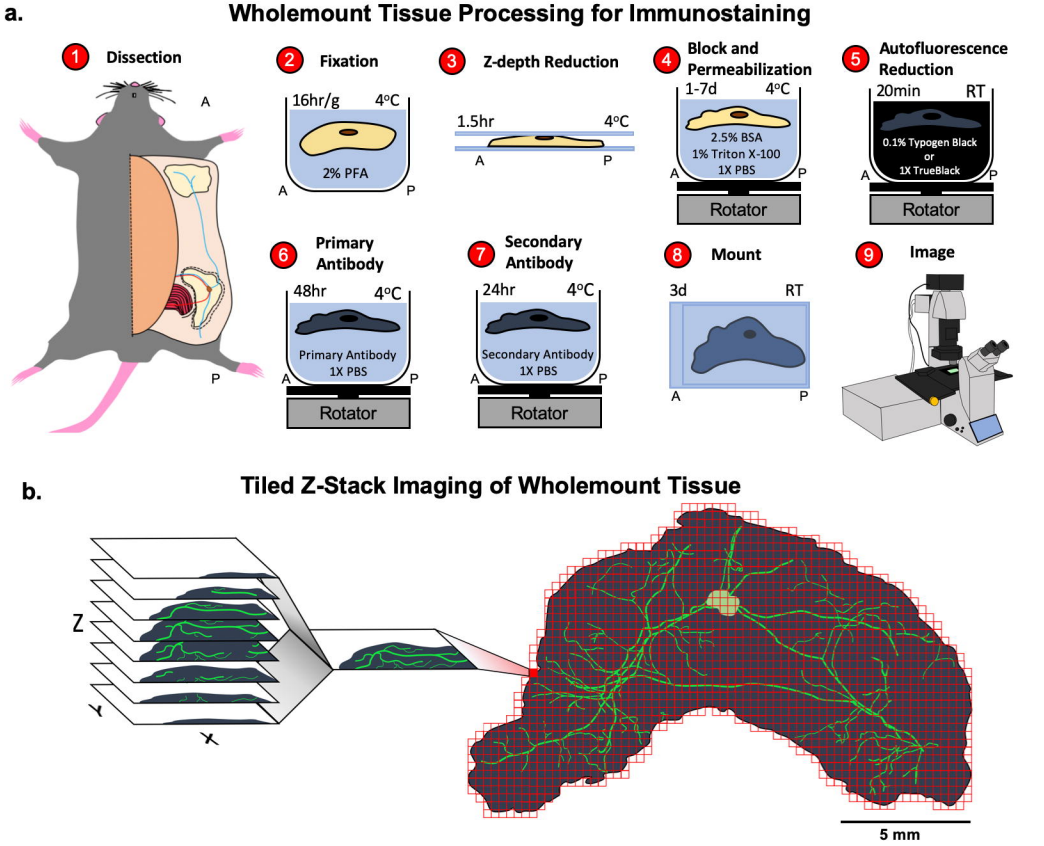

Tissue Processing and Imaging:
dx.doi.org/10.17504/protocols.io.6nzhdf6
Quantification:
https://github.com/ktownsendlab/willows_et_al-2019

Figure 2: Reduction of adipose tissue autofluorescence and depth coding

a.

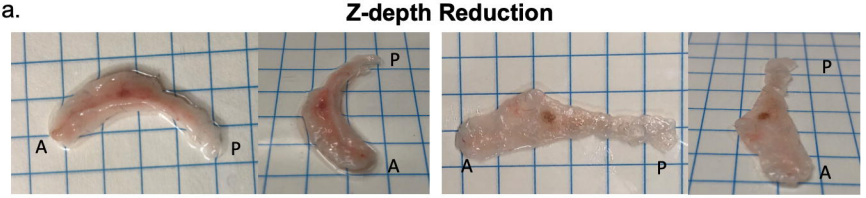

b.

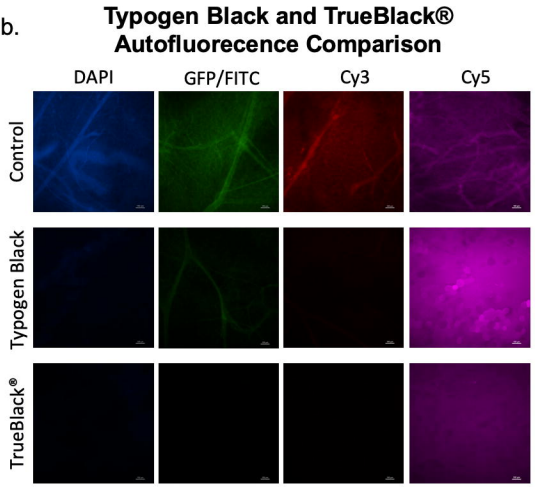

c.

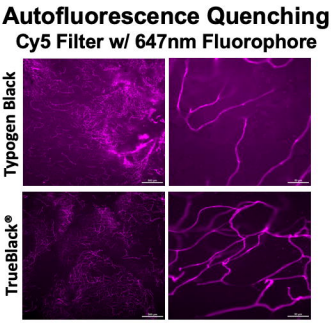

d.

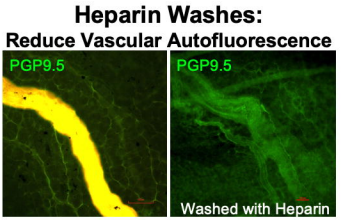

e.

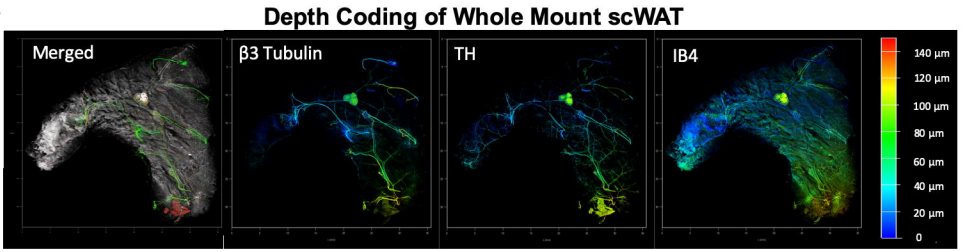

f.

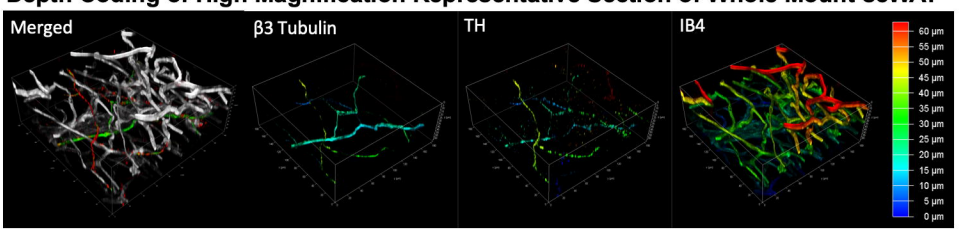

Figure 3: Whole depot neurite quantification following cold challenge

a. Cold Exposed Whole Depot Axillary scWAT

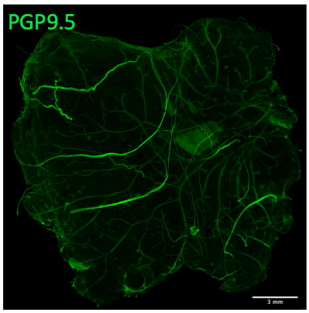

RT

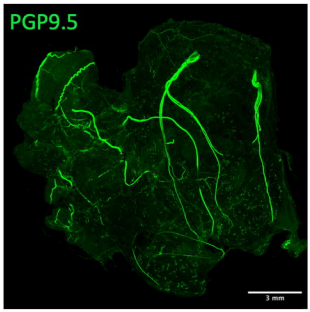

7 day 5°C

b. Axillary scWAT Neurite Density

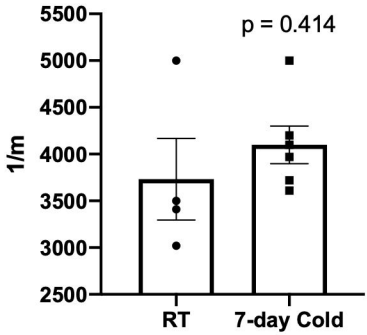

c.

Neurite Density Heatmap

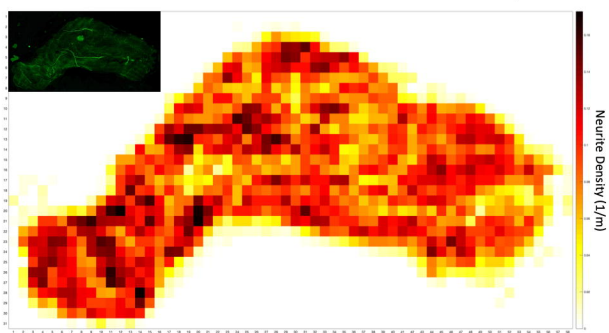

i-scWAT

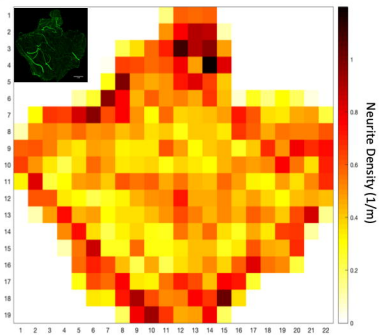

a-scWAT

Figure 4: Peripheral innervation of inguinal scWAT

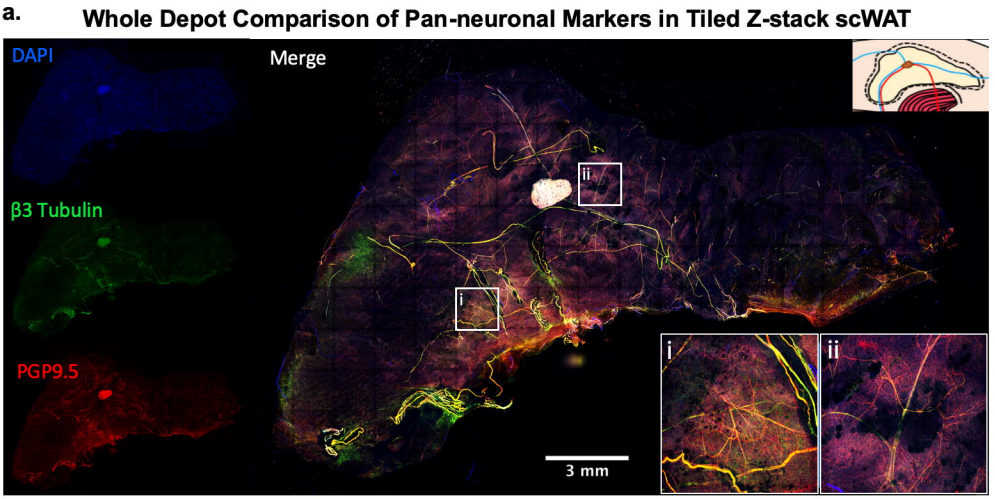

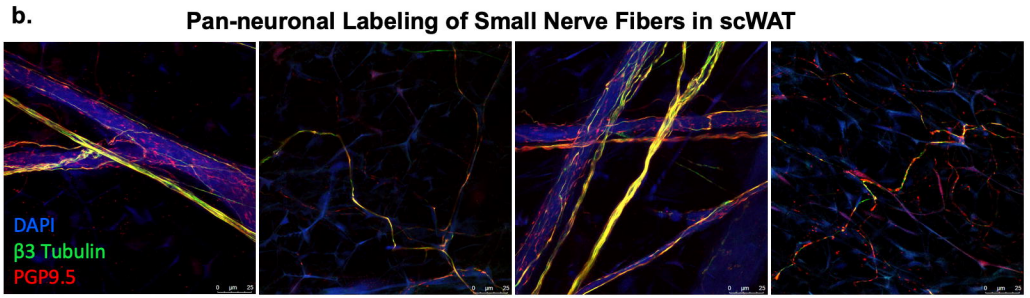

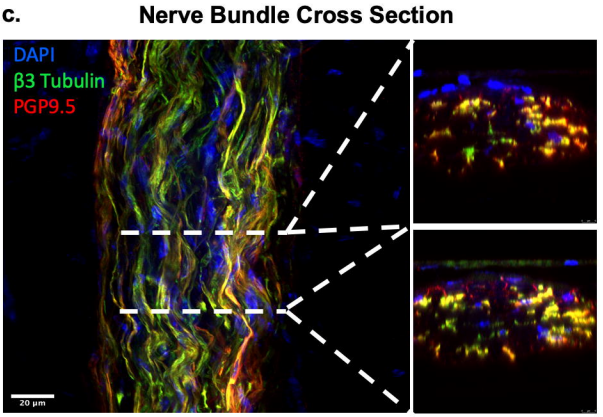

Figure 5: Characterization of whole depot inguinal scWAT nerves

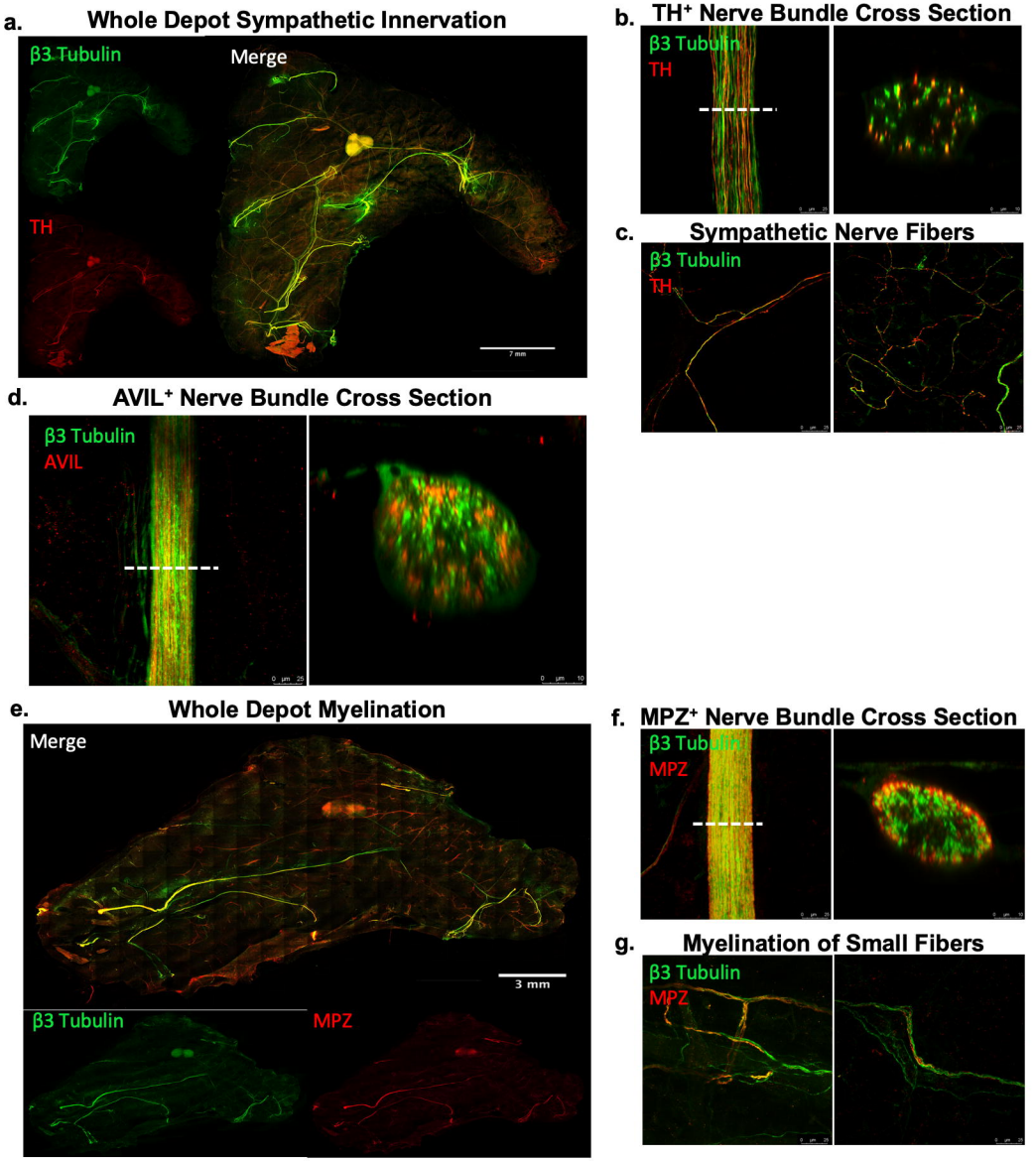

Figure 6: Neurovascular interaction within whole mount inguinal scWAT depot

a. Whole Depot Neurovascular Stain

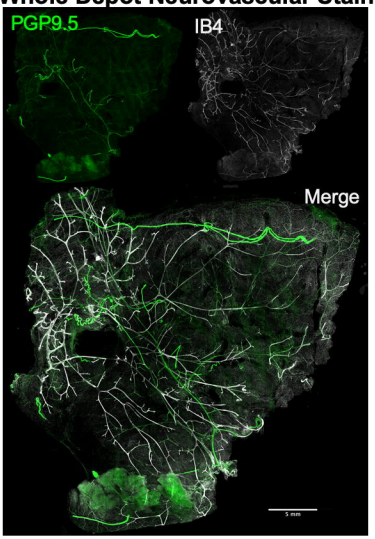

b. Categories of Neurovascular Interactions in scWAT

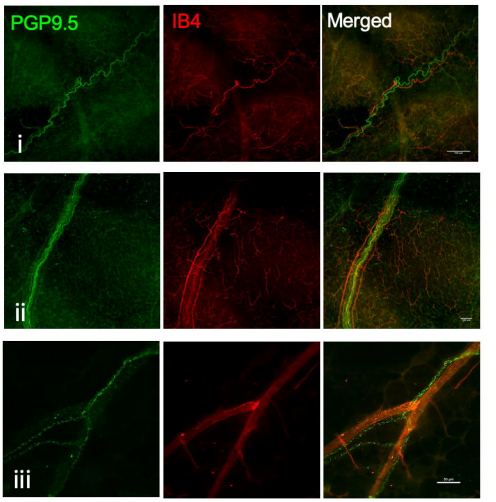

c. SNS Innervation of scWAT Vasculature

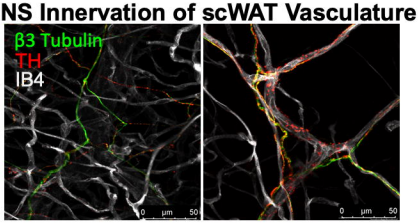

d. scWAT Vasa Nervorum

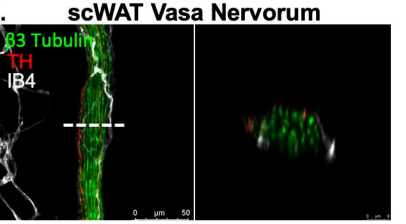

e. scWAT Perivascular Sympathetic Plexus

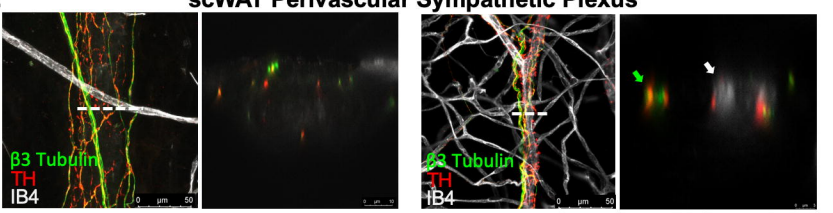

Large Diameter Vessel

Small Diameter Vessel

f. Myelinated Nerve Fibers Around scWAT Vasculature

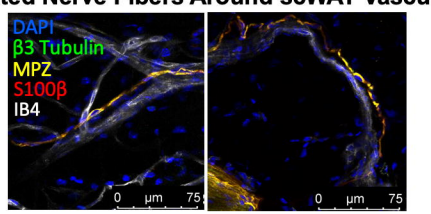

Figure 7: Second harmonic generation imaging of collagen in BTBR$^{+/+}$ (WT) and BTBR$^{ob/ob}$ (MUT) inguinal scWAT

a.